Open Research Online

Electron multiplication CCD detector technology advancement for the WFIRST-AFTA coronagraph

Conference or Workshop Item

For guidance on citations see FAQs.

Version: Version of Record

Link(s) to article on publisher's website:
http://dx.doi.org/doi:10.1117/12.2189927

oro.open.ac.uk

Electron Multiplying CCD Detector Technology Advancement for the WFIRST-AFTA Coronagraph

Leon K. Harding[1,a], Richard T. Demers[a], Michael Hoenk[a], Pavani Peddada[a], Bijan Nemati[a], Michael Cherng[a], Darren Michaels[a], Anthony Loc[a], Nathan Bush[b], David Hall[b], Neil Murray[b], Jason Gow[b], Ross Burgon[b], Andrew Holland[b], Alice Reinheimer[c], Paul R. Jorden[d] and Douglas Jordan[d]

[a]Jet Propulsion Laboratory, California Institute of Technology, 4800 Oak Grove Drive, Pasadena 91109, CA, USA;
[b]Center for Electronic Imaging, Department of Physical Sciences, The Open University, Walton Hall, Milton Keynes, MK7 6AA, UK;
[c]e2v inc., 765 Sycamore Drive, Milpitas CA 95035, USA;
[d]e2v technologies, 106 Waterhouse Lane, Chelmsford, Essex, CM1 2QU, England

ABSTRACT

The WFIRST-AFTA (Wide Field InfraRed Survey Telescope-Astrophysics Focused Telescope Asset) is a NASA space observatory. It will host two major astronomical instruments: a wide-field imager (WFI) to search for dark energy and carry out wide field near infrared (NIR) surveys, and a coronagraph instrument (CGI) to image and spectrally characterize extrasolar planets. In this paper, we discuss the work that has been carried out at JPL in advancing Electron Multiplying CCD (EMCCD) technology to higher flight maturity, with the goal of reaching a NASA technology readiness level of 6 (TRL-6) by early-to-mid 2016. The EMCCD has been baselined for both the coronagraph's imager and integral field spectrograph (IFS) based on its sub-electron noise performance at extremely low flux levels - the regime where the AFTA CGI will operate. We present results from a study that fully characterizes the beginning of life performance of the EMCCD. We also discuss, and present initial results from, a recent radiation test campaign that was designed and carried out to mimic the conditions of the WFIRST-AFTA space environment in an L2 orbit, where we sought to assess the sensor's end of life performance, particularly degradation of its charge transfer efficiency, in addition to other parameters such as dark current, electron multiplication gain, clock induced charge and read noise.

Keywords: EMCCD, WFIRST-AFTA, Radiation Damage

1. INTRODUCTION

WFIRST-AFTA will make use of an existing 2.4 m telescope and will advance what is currently possible in exoplanet spectral characterization and imaging by achieving contrast of order 10^{-9} for cold Jupiters, mini-Neptunes and super Earths compared to their host stars. This spectroscopic characterization will reveal the atmospheric composition of such planets and will be used to search for spectral signatures of life. In addition, the coronagraph will be used to probe planetary formation via characterization of debris disks in and around planetary orbits. The CGI will operate in two modes: i) a Hybrid Lyot Coronagraph (HLC) for exoplanet photometry and discovery and ii) a Shaped Pupil Coronagraph (SPC) for exoplanet spectroscopy and debris disk characterization. In order to maintain contrast stability, a Low Order WaveFront Sensor (LOWFS) and control system in the coronagraph is used to sense and correct lower order wavefront error resulting from i) thermally induced optical misalignment and optical surface distortions and ii) Line of Sight (LOS) jitter caused by vibration sources such as the spacecraft reaction wheels and the WFI cryocooler; see Demers et al. (2015)[1] for more information on the optical layout for the HLC and SPC, and the LOWFS.

The CCD201-20 EMCCD, an e2v sensor, has been baselined for the AFTA CGI – both the imager and IFS. However, prior to its selection and in order to fully assess the signal to noise (S/N) performance of the EMCCD,

---

[1]Corresponding author: Leon.K.Harding@jpl.nasa.gov

Table 1. Detector candidate technologies for JPL trade study. The read noise performance quoted are nominal values from respective studies that were released. The 'Limitations' column refers to either a non-optimal design detail for the WFIRST-AFTA CGI, or to some test or study that has not yet been carried out. We note that at the time of the trade study, the CCD201-20 had not been radiation tested.

Short Name	Mission	Detector Model/N	Manuf.	TRL	Pixel (μm)	Full Format (pixel)	Limitations
sCMOS	Ground-based	CIS2051	Fairchild Imaging	4	6.5×6.5	2560×2560	Lowest TRL No rad./therm. cycling No temp data
Euclid CCD	Euclid vis. instrument	CCD273-84	e2v	6	12×12	4096×4096	RN $\sim$3.5 e$^-$
HST CCD	HST WFC3	CCD43	e2v	9	15×15	2050×4096	RN $\sim$3 e$^-$ Std epi depth
Gaia CCD	Gaia	CCD91-72	e2v	9	30×10	1966×4500	RN $\sim$6 e$^-$ Unfavorable format
JMAPS HyViSI	JMAPS	HiViSI	Teledyne	6	18×18	1024×2048	RN $\sim$5 e$^-$
EMCCD Std AN	WFIRST-CGI	CCD201-20	e2v	5	13×13	1024×2048	Low TRL No therm. cycling
EMCCD DD AN	WFIRST-CGI (DD)	CCD201-20	e2v	2	13×13	1024×2048	Thin epi (std)

Acronyms: TRL=Technology Readiness Level; RN=Read Noise.
HST=Hubble Space Telescope; WFC3=Wide Field Camera 3; DD=Deep Depletion.
Abbreviations: Std=Standard; AN=Analog; Rad./Therm. =Radiation/Thermal; pix=pixel.

it was compared to other candidate sensors that also exhibited reasonably good performance (but may also have higher flight heritage and/or higher technological maturity) in a separate detector trade study. These candidates, which were considered to be principal low light level detector technologies, were evaluated and ranked based on: 1) compliance with performance requirements for the Imager and IFS detectors, 2) flight heritage, 3) desired format and pixel pitch, and 4) planet yield predicted by a coronagraph model. The trade study was comprised of seven specific detector models from four competing technologies. The seven candidates were:

1) Monolithic scientific CMOS.

2) Conventional CCDs as used in EUCLIDs visible focal plane array.

3) Conventional CCDs as used in HSTs Wide Field Camera 3 (WFC3).

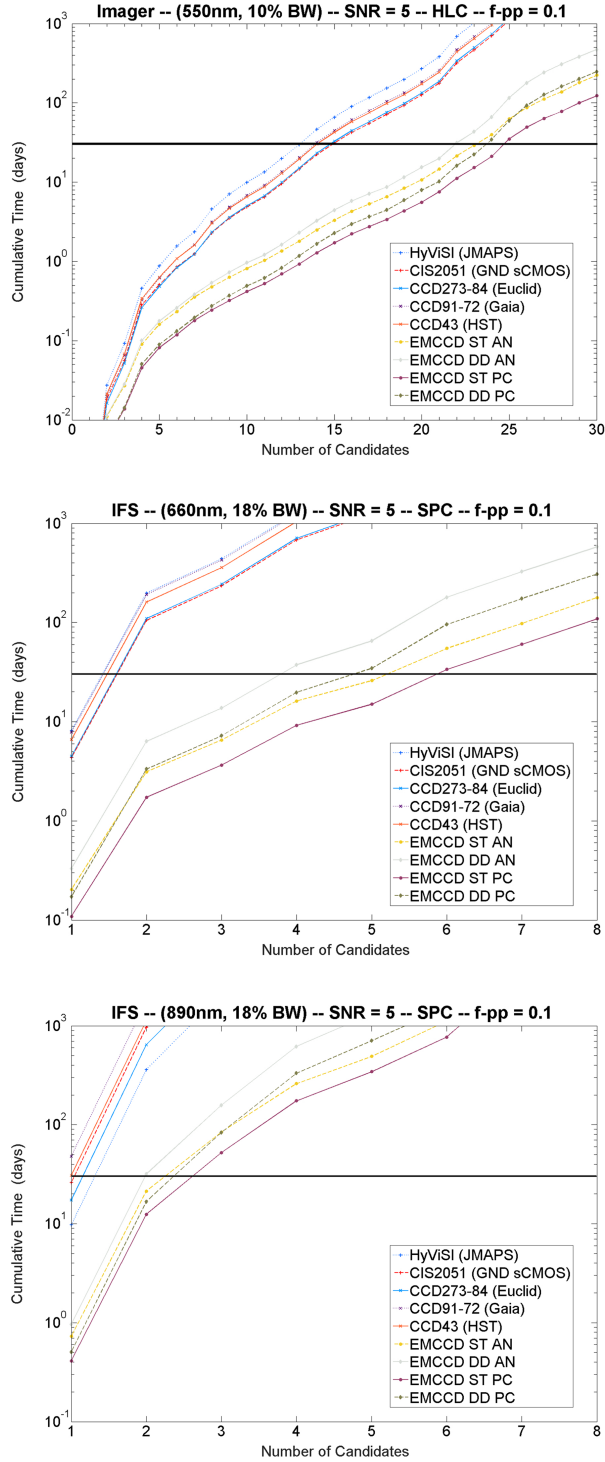**4)** Deep depletion (DD) CCDs as used in Gaia's large Astrometric Focal Plane (AFP; Kohley et al. 2012[2]).

Figure 1. Analytical prediction of observation time required to achieve S/N=5 versus the number of planets for each of the detector candidates. Top: 550 nm 10% Imager band (HLC), Middle: 660 nm IFS 18% band (SPC); Bottom: 890 nm IFS 18% band (SPC). f−pp denotes the post-processing residual error and is assumed to have a value of 0.1 consistent with contrast improvement (reduction) of a factor of ten. The horizontal black line indicates a 30 day threshold.

5) Hybrid Silicon CMOS arrays as used in Hybrid Visible Silicon Imager (JMAPS) focal plane array.

6) Standard silicon-thickness EMCCD operated in analog electron multiplication (EM) gain mode and photon counting mode.

7) DD EMCCD operated in analog EM gain mode and photon counting mode.

To evaluate the relative science yield of the candidate detectors we simulated end-to-end CGI performance using each of seven specific detector candidates. The model predicted the time required to collect images and spectra of planets from a list of known radial velocity planets. The predicted observation time was calculated as the time required to achieve a S/N of 5 for either planet imaging or spectroscopy. The model showed that for the expected science targets, we expect the IFS detector to detect a mean signal on the order of 3×10^{-3} e^{-} pix^{-1} sec^{-1}. We show each candidate and its basic properties in Table 1 and the model results of the study in Figure 1. Based on this study, we found that both the standard thickness and DD EMCCD outperformed all other detector candidates, providing the highest S/N and planetary yield estimate for the AFTA CGI projected mission lifetime. We note that the standard thickness EMCCD was chosen over a DD EMCCD variant, since it is a standard product fabricated in medium volume for commercial applications and therefore has well characterized yield and low fabrication process risk. Furthermore, e2v has never fabricated the CCD201-20 with DD silicon and therefore selection of this device would entail risks of low fabrication yield or low device operability. Additionally, a DD device cannot be run in inverted mode operation (IMO), therefore dark current contribution is significantly higher and far out-weighs the benefit of greater QE response in the NIR, consistent with the predictions in Figure 1.

Please see Harding et al. (2015)[3] for a complete discussion of the trade study, the parameters used for each technology and the selection criteria that were implemented to ultimately choose the EMCCD as the CGI detector.

2. WHAT IS AN EMCCD?

The architecture of an EMCCD (Jerram et al. 2001,[4] Hynecek 2001[5]) is very close to that of conventional CCD technology. The difference is in the EMCCD's high gain register which is an extended multiplication stage containing a large signal output that lies after the conventional serial register. It is in this region where electrons can be amplified by the presence of high local electric fields by a process known as avalanche multiplication. Crucially, this process is inherently stochastic, where there is $\sim 1 - 1.5\%$ probability of an extra electron getting generated per signal electron per given multiplication stage. Since a device can contain hundreds of multiplication stages, the probability of amplification becomes significant, and the subsequent EM gain can amplify the signal by factors of thousands. This process ultimately produces sub-electron effective read noise performance over a wide range of read out rates, thus resulting in a much higher S/N, albeit at the proportional reduction in pixel charge handling capacity. We note that there is an added variance in the EM output that consequently reduces the S/N, that results in an effective reduction of the sensor's QE by up to $\sim 50\%$. This is referred to as the "Excess Noise Factor" (ENF); however, post-read out techniques can reclaim this reduction in QE (Daigle et al. 2008[6]).

The CCD201-20 sensor (hereafter CCD201), baselined as the AFTA CGI detector, is a 2-phase, frame transfer (FT) device, and has dual output amplifiers. It has an image section of 1024×1024 active pixels with a store section of 1056×1037 pixels, where thinning and back-illumination help to improve QE, peaking at >90% at 550 nm – assuming the standard midband e2v coating, see: http://www.e2v-us.com/products/imaging/qe-curves/. The full spectral range (>15% QE transmission) of the sensor lies between $\sim 300 - 1000$ nm, allowing tests in all AFTA-C Imager and IFS bands. The CCD201 can provide a maximum well depth of 80,000 e^{-} in the image section and 730,000 e^{-} in the gain register. Pixels in the gain register are designed to have a large full well capacity in order to avoid saturation during readout.

Evaluating the S/N in an EMCCD is much like that of a normal CCD; however, since there is a gain factor applied during the amplification process, the read out noise is reduced by $\frac{R}{G}$, where R is number of electrons

Table 2. Specifications of the CCD201-20 EMCCD, from e2v.

Parameter	Specification
Sensor family	EMCCD
Variant	BI[*], 2-Phase
Active pixels (image)	1024 (H) × 1024 (V)
Frame Transfer (store)	1056 (H) × 1037 (V)
Image area	13.3 mm × 13.3 mm
Pixel pitch	13 μm
Active area CHP[†]	80,000 e- pix^{-1}
Gain register CHP[†]	730,000 e- pix^{-1}
Fill factor	100%
# O/P amplifiers	1 × Conv., 1 × EM
Multiplication elements	604
Dark reference columns	32
Overscan elements	16

[*]BI = Back-Illuminated; [†]CHP = charge handling capacity.

and G is the amplification gain. However, as outline above, there is an added variance in the signal – the ENF. Therefore, when calculating the S/N for an EMCCD, the read noise becomes negligible but the ENF and multiplication gain must be included, in addition to other standard parameters such as the quantum efficiency, QE, and the total signal in photoelectrons, S, where $S = P \cdot QE \cdot t$. The terms P and t are the incident photons and integration time, respectively. The principle sources of noise are found via the root of sum of squares law and the S/N equation is thusly calculated as shown (adapted from McLean et al.[7]):

$$S/N = \frac{S}{\sqrt{2S + (\frac{R}{G})^2}},\tag{1}$$

where S becomes $2S$ in the denominator representing the noise, because of the ENF adds to the photon shot noise where the uncertainty now becomes $\sqrt{2S}$ as opposed to $\sqrt{S}$ (ENF= $1.41^2 \sim 2$). Most importantly, although the read noise gets reduced by $\frac{R}{G}$, the pixel charge handling capacity will also be reduced by this same factor.

Standard properties of the CCD201 are shown in Table 2 and the results presented in this work for the beginning of life (BOL) and end of life (EOL) performance were carried out with a standard thickness CCD201 EMCCD.

3. DETECTOR TECHNOLOGY DEVELOPMENT PLAN

Under NASA pre-phase-A technology development funding, JPL is moving forward the technological maturity of the CCD201 for space flight in order to reach NASA TRL-6. Following meeting detector performance requirements for its BOL, a three-part program to advance the device maturity is underway, consisting of 1) radiation environment testing, 2) noise performance optimization and 3) thermal environment testing.

3.1 Radiation Environment Testing

Phase I: In the first of a two-phase radiation test, the radiation hardness of a pair of CCD201 engineering grade devices at ambient temperature was characterized after having been irradiated by a single exposure Displacement Damage Dose (DDD) representative of a six year mission with direct insertion to L2 orbit. The result is also relevant to a potential geosynchronous orbit, as explained in Section 4. This first phase was carried out to provide an early indication of survivability of the CCD201 in the L2 radiation environment since no EMCCD has yet been qualified or flown in space and, as mentioned above, a large format EMCCD of this design has not yet been radiation tested. The results of Phase I are relevant to a mission in which periodic warm cycling of

the coronagraph EMCCDs would be conducted to reverse some of the radiation induced damage. The results of Phase I are presented in Section 5.2.

Phase II: For the second phase of radiation testing, the CCD201 will remain operational and will be maintained at cold operating temperature (165 K) while being subjected to multiple DDDs with a cumulative dose equal to the six-year mission life at L2. The device performance will be characterized before and after each of the four separate proton doses in order to provide information on the rate of performance degradation throughout the six-year lifetime. The results of Phase II testing will provide a worst-case test of radiation hardness, representing flight operation over six years without the benefit of in-flight warm cycling or any longer term annealing that may occur over time at this colder temperature.

We note that although Michaelis et al. (2013)[8] carried out a DDD study of the CCD201, the device was operated at 5 frames per second for signal levels of 10 e$^-$, with multiplication gain of 100. Since the effects of radiation can greatly affect a device in different ways based on its operating conditions (discussed later in Section 5.2), we conducted the Phase I study as a survivability test for the CCD201 specifically for the AFTA application. Therefore, the sensor was run under higher gain conditions (by a factor of 2), for both high flux (>1600 e$^-$) and low flux (∼8 e$^-$) signals, and for an integration time of 100 seconds. This test plan was important based on the disparate operating modes of the AFTA CGI. In Phase II, the CCD201 will be irradiated over the full range of proton fluences reflecting BOL to EOL for L2, whilst kept at cryogenic temperatures in the beamline, where the device will be under power at all times in order to measure flat-band shifts as expected in flight. This will be the first time that a CCD201 is subjected to this kind of radiation test.

3.2 Performance Optimization

Proton radiation results in the creation of charge traps which reduce the EMCCD charge transfer efficiency (CTE). The CTE can also be written as 1 – CTI, which is the 'charge transfer inefficiency'. We will use the CTI term for discussion of this phenomenon for the remainder of this manuscript. Techniques such as pocket pumping (see: Janesick 2001,[9] Hall et al. 2014,[10–12] Wood et al. 2014,[13] and Murray et al. 2012[14, 15]) will be used to characterize the traps in the post-irradiation EMCCDs. Once characterized, various operational mitigation techniques such as charge injection and various clock waveforms will be used to optimize the performance in the presence of charge traps (Gow et al. 2012[16]). In addition, post processing correction algorithms (Massey et al. 2014[17]) will be tested.

3.3 Thermal Environment Testing

The CCD201 will undergo multiple thermal cycles spanning the mission survival temperature range and the resulting performance degradation will be characterized. A device will also undergo a 24 hour thermal soak at the warm and cold survival temperature extrema.

4. THE WFIRST-AFTA CGI SPACE ENVIRONMENT

4.1 The Geosynchronous/L2 Environment

As part of the current design cycle (Cycle 6) the WFIRST-AFTA project is carrying out a trade between a geosynchronous orbit and an L2 orbit similar to that of the James Webb Space Telescope (JWST). If the project selects the L2 orbit, it is most likely to be a direct insertion orbit whose trajectory through the Earth's trapped-particle radiation belts will be very short and inconsequial. Therefore, the exposure to harmful radiation in general is lower at L2 compared to geosynchronous orbit.

To calculate the radiation environment for the AFTA CGI detector in L2, we ran the radiation transport computer code, NOVICE (Jordan et al. 2006[18]), for a geosynchronous orbit and subsequently removed the contribution from the Earth-trapped protons and electrons, leaving only the solar proton fluence, common to both geosynchronous and L2 orbits. This was verified by comparing model results to predicts for the JWST space mission from the Goddard Space Flight Center (GSFC) model where each result was in agreement. These data were calculated based on the JPL 91 Solar Proton model at a 95% confidence level and with a radiation
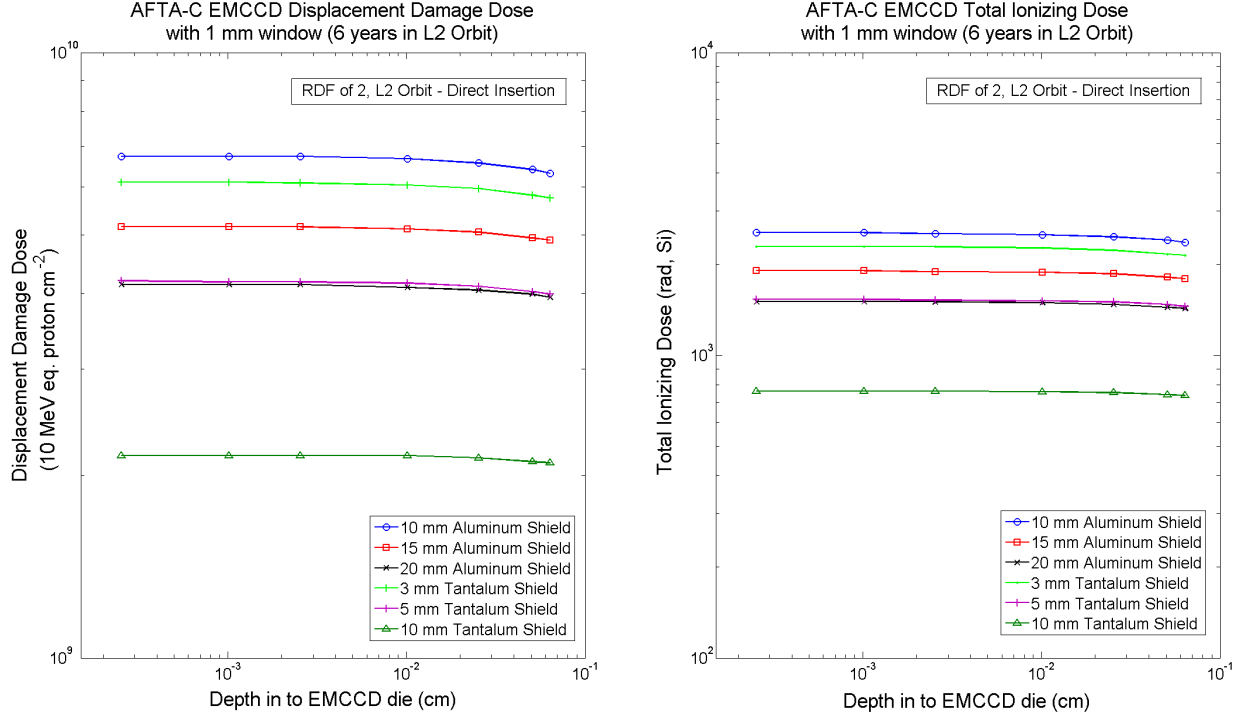
Figure 2. *(Left)* Logarithmic plots of DDD (10 MeV equivalent protons cm^{-2}) as a function of depth in the EMCCD (cm) with a 1 mm-thick glass window. This is for an L2 orbit (direct insertion) for an RDF=2. DDD is shown for a range of various shielding materials and thicknesses. *(Right)* Logarithmic plots of TID (rad, Si) as a function of depth in the EMCCD (cm) with a 1 mm-thick glass window. This is for an L2 orbit (direct insertion) for an RDF=2. TID is shown for a range of various shielding materials and thicknesses.

design factor (RDF) = 2. NOVICE was used to calculate DDD and total ionizing dose (TID) in the EMCCD die. A simple 3D mass model of the EMCCD package and radiation shield CAD design (cylindrical drum shield) was used for the radiation transport calculation. To assess the DDD and TID in the CCD die, seven "dose detectors" along the CCD die center perpendicular line were selected. Thus, the dose levels were calculated at the detector surface and bulk depths of 2.54 μm, 10.16 μm, 25.4 μm, 101.6 μm, 254 μm, 508 μm and 640 μm.

Figure 2 shows the expected radiation exposure of the AFTA CGI detectors over the span of a 6 year mission in L2 orbit, for both DDD and TID, respectively, for a range of tantalum and aluminum shielding thicknesses and including a 1 mm thick glass window placed in front of the detector. We note that the design for the EMCCD shielding material and thickness will later be refined based on the results of the Phase II radiation testing. The DDD radiation doses to be used in Phase II will span the radiation levels across the family of curves shown in Figure 2. In Phase II we will measure the detector performance degradation as a function of DDD fluence. Then, the shielding material and thickness will be chosen to correspond to an acceptable EOL performance degradation.

The model revealed that there is a significant difference between geosynchronous and L2 orbits for the damage due to TID, whereas there is negligible difference between the two orbits for the damage due to DDD. Using the radiation model it was determined that a 1 mm thick glass window in front of the EMCCD reduced the TID level in the surface layer to only 1 krad (RDF=2) for a radiation shield of 10 mm thick tantalum. Based on these results, since TID will be reduced to very low levels, DDD was identified as the primary risk to EOL detector performance; thus, in this work, we explore the effects of DDD only.

4.2 Displacement Damage

CCDs have been extensively developed and applied for precision measurements in space, beginning with NASA's Galileo spacecraft and the HST, and continuing to the present with large focal planes on Kepler, Gaia and Euclid.

7

Radiation environments in space and their effects on detectors have been extensively studied, and NASA/JPL have developed tools for modeling and testing the effects of such environment on CCDs (see Janesick 2001,[9] and references therein). Despite the extensive heritage of silicon detectors in space, there is at present no flight-proven detector technology that meets AFTA CGI requirements. Importantly, as noted previously, although there have been other studies of radiation affects on EMCCDs (Michaelis et al. 2013[8]), no EMCCD has been tested to a radiation environment that reflects the AFTA CGI space conditions. See Harding et al. (2015)[3] for a more in-depth discussion on CCD radiation damage.

4.2.1 Trapping

Energetic particles such as protons and neutrons can damage detectors by displacing silicon atoms from their lattice sites in the silicon crystal. Silicon vacancies are associated with energy levels in the silicon bandgap, which can capture photo-generated electrons and holes. One effect of traps is therefore a degradation of detector sensitivity and increased noise, as trap-assisted generation and recombination events cause a loss of signal and increase the bulk dark current. The greatest impact of displacement damage on detector performance comes from the smearing of charge that results from trapping and subsequent detrapping of electrons, leading to artifacts such as image persistence and deferred charge.

4.2.2 Trap Species & Characterization

Isolated vacancies in silicon are unstable, and vacancies will migrate through the crystal until they interact with other defects to form a stable configuration. The most common trap species in radiation-damaged silicon are divacancies, phosphorus-vacancy complex, and oxygen-vacancy complex. Each of these forms a distinct set of trap states in the silicon.

Once the trap properties are known, the dynamics of electron trapping and detrapping events can be modeled using Shockley-Read-Hall theory (Shockley & Read 1952[19]). The degradation of CCD performance depends not only on the density, location, and types of traps present in the detector, but also on CCD operating parameters such as detector temperature, bias voltages and clock frequencies. If these parameters can be measured and/or calibrated, it becomes possible to correct for trap-induced errors using image post-processing algorithms. Deferred charge can be corrected on the HST to a precision of 97%, and work is ongoing to improve correction algorithms to achieve 99% accuracy for the ESA Euclid mission. Image correction algorithms run into limitations at low signal levels. For example, even with perfect knowledge of the trap locations and properties, capture and emission times for trapping/detrapping events are stochastic, so that the accuracy that can be achieved by image correction algorithms depends on the number of photons detected (Hall et al. 2014,[10, 12, 20] Massey et al. 2014,[17] Israel et al. 2014[21]).

5. RESULTS

5.1 CCD201-20 Performance: Beginning of Life (BOL)

BOL testing of the CCD201 was carried out over a range of temperatures with a Nüvü Cameras EMN2 system and the CCCP controller (hereafter EMN2; see: http://www.nuvucameras.co-m/products, for product details) using both the conventional and EM outputs as well as all combinations of vertical clocking frequencies and horizontal read out rates that the EMN2 offered. This characterization work included testing for the primary sources of noise such as read noise, dark current and clock induced charge. The device was run in IMO for maximum dark current performance, and the serial register was run in its standard non-inverted mode (NIMO) in order to minimize clock induced charge (CIC). The $R\phi 2HV$ ("high voltage clock") voltage was adjusted where necessary in order to change the multiplication gain applied. We used multiplication gains of $\times 1000$ for dark current measurements with the EM register, and for all CIC measurements. This reduced the effective read out noise to sufficiently low levels so that CIC and other spurious noise could be assessed. It also allowed for much shorter integration times for dark current frames. All dark current data were taken under zero illumination conditions. We followed standard practices as outlined in Janesick (2001)[9] for the assessment of each parameter.

We show the BOL AFTA CGI detector requirements in Table 3, as well as the results from our BOL characterization of the CCD201 that was carried out at JPL with the EMN2 camera. As shown, the EMCCD has met all requirements for read noise, dark current and CIC. We used a parallel frequency of 1 MHz and a serial

Table 3. AFTA CGI beginning of life (BOL) performance for the CCD201-20 EMCCD as measured on the EMN2 camera system at JPL. We have included a column for the goal, requirement and measurement. The requirement field reflects the performance that was used in the detector trade study, see Figure 1, and the measurement is from this work. The goal field was created to give further margin on the detector's fundamental performance, in the event that other effects such as those related to radiation damage may dominate in later studies. Note: A = area, T = temperature, IMO = inverted mode operation and G = gain factor.

Specification	Goal	Requirement	Measurement	Unit	Notes
Active Pixels	...	1024×1024	...	Pixel	...
Pixel Pitch	...	13×13	...	mm	$A = 177.2 \text{ mm}^2$
Eff. Read Noise	0.2	0.2	<0.2	e$^-$	With EM gain
Dark current	1×10^{-4}	5×10^{-4}	1.01×10^{-4}	e$^-$ pix^{-1} sec^{-1}	$T = 188$ K, IMO
CIC	1×10^{-3}	1.8×10^{-3}	1.7×10^{-3}	e$^-$ pix^{-1} fr^{-1}	10 MHz serial rate, $G = 1000$

read out frequency of 10 MHz for all results in Table 3. Since the native read out noise of the CCD201's EM amplifier at 10 MHz using the EMN2 was measured to be $\sim$90 e$^-$ rms, we used a gain factor of $\sim$450 to achieve an effective read out noise of 0.2 e$^-$ rms.

The AFTA CGI dark current requirement, which is based on the planetary models described in Section 1, is 5 $\times$ 10^{-4} e$^-$ pix^{-1} sec^{-1}, which reflects a dark current at 188 K. Since the projected AFTA CGI observation time is currently of order $100 - 300$ seconds, it is vital that dark current is minimized as much as possible. As will be shown in the next section, we believe that an order of magnitude lower contribution can be achieved by further cooling the sensor from 188 K to 165 K and running in IMO; however, it has been shown that for temperatures < 188 K, CTI can occur under high gain conditions possibly as a result of charge clouds interfacing with surface states. This might cause smearing of cosmic rays or other particles given sufficient energy.

CIC also met the AFTA CGI requirement of 1.8×10^{-3} e$^-$ pix^{-1} fr^{-1}, where we measured 1.7×10^{-3} e$^-$ pix^{-1} fr^{-1} at a 10 MHz serial clocking frequency. We note that it can be difficult to disentangle CIC and dark current, in addition to other sources of noise in a detector. However, since the CIC can vary strongly as a function of clock swing, clock rise time as well as the device bias conditions (in addition to waveshapes, as reported by Daigle et al.[6]), it is thus heavily dependent on the clocking process and how these parameters are designed in order to transfer charge (Janesick 2001[9]). Indeed, careful consideration of a device's clocking design also minimizes the CTI. These parameters are still being considered to further optimize the device for the AFTA CGI application. We refer the reader to Harding et al. (2015)[3] for further discussion on all concepts above, in addition to other considerations such as persistence, clocking modes and manufacturer design modifications.

5.2 Radiation Study of CCD201-20: End of Life (EOL)

5.2.1 Phase I Irradiation Plan

In Section 1, we outlined a two-phase radiation study to investigate DDD damage on the performance of the CCD201. In this section, we present the results of Phase I, where an ambient temperature, unbiased, irradiation was carried out at the Proton Irradiation Facility (PIF), at the Paul Scherrer Institute (PSI), in Switzerland, on Feb 23, 2015, and post-irradiated analysis carried out by the Centre for Electronic Imaging (CEI) at the Open University in the UK. This study was designed to include full sensor characterization of two engineering grade CCD201 devices at ambient temperature. It should be noted that although these devices are considered engineering grade, we consider the measured performance in this study post-irradiation as representative of what scientific grade sensors will experience, since this study sought to investigate a degradation factor on performance for each characterization parameter. These parameters include: multiplication gain, dark current, CIC, high flux parallel and serial CTI as well as low flux parallel and serial CTI, before and after a radiation dose of 2.5 $\times$ 10^9 protons cm^{-2} (10 MeV equivalent). See Bush et al. (2015)[22] for details on PSI beam intensity profile and dosimetry. This dose reflects the EOL dose (6 yr in L2) for a 10 mm tantalum shield. Phase II commenced in June, 2015 and was completed in August, 2015, which covered the full range of doses for all shielding variants

and thicknesses (Figure 2), where a custom apparatus has been designed and built to maintain device cryogenic temperatures throughput the study. We will briefly outline the Phase II study later in this section but here we present results from Phase I only.

We selected irradiated regions of each device thereby ensuring a control region for both parallel and serial registers – this allowed the independent and combined effects of radiation-induced displacement damage on parallel and serial CTI to be investigated in a way that prevented contamination. Monte-Carlo simulations were performed using the Stopping Range of Ions in Matter (SRIM) package (Ziegler et al. 2010[23]). These simulations provided the maximum penetration depth of the beam as it passes through stainless steel (the element used for shielding), which was ∼9 mm, thus a thickness of 14 mm was used for redundancy.

For device one, the shielding profile was designed such that the degradation of parallel performance could be evaluated where the serial registers were protected. Additionally, the right side of the parallel section was also protected and used as a control region, where results from this section were expected to be identical to those prior to irradiation. The shielding profile in device two allowed the effects of radiation damage to be assessed on both the serial and parallel sections, as well as these sections combined. In this way, charge getting transferred through the right side of device two should get affected in the serial direction only. Note that in device two, a small region of the parallel section in the control region (right side) was irradiated - this is because the serial register is small when compared to the store and image sections, and therefore irradiating a small region (∼300 pixels) of the parallel section ensured that the serial register was fully irradiated.

5.2.2 Experimental Setup

All pre- and post-irradiation tests were carried out at 165 K with a frame integration time of 100 seconds (unless otherwise stated) and the devices were run in IMO. The CCD was operated using generic drive electronics for test and characterization from XCAM Ltd. (www.xcam.co.uk), consisting of a 19″ rack-based controller, together with proximity electronics on a headboard PCB local to the CCD, providing bias filtering and low noise pre-amplification. The control electronics used for testing were standard and thus were not fully optimized to match those of the EMN2 described earlier sections. We note that the use of this controller does not invalidate this test, since we sought to identify performance degradation of the CCD201 only – this does not include controller or other proximity electronics. While some parameters will change based on the camera controller used (e.g. read out rate), the trends exhibited due to radiation damage in this study should be independent of the CCD controller. Part of the study's strategy was to keep pre- and post-irradiation controller operating conditions identical. We felt that it was important to initially separate the device and the controller so that we could interpret results in the context of the EMCCD only. A further study will be initiated in order to investigate the effects of such radiation on a custom-developed EMCCD controller – the initial designs of which have been initiated at JPL. This study can then assess the controller in a relevant environment to the AFTA CGI.

The XCAM setup enabled rapid investigation of the pre- and post-performance of the device. We used the default read out modes for clocking through the large signal (LS) amplifier, and bias signals as recommended by e2v (see: www.e2v-us.com/products/imaging/imaging-sensors-cmos-ccd-emccd) were used with the device image and store sections being operated in 2-phase mode. Some minor modifications were made based on pre-characterization tests in order to minimize the read out noise and a read out pixel rate of 700 kHz and parallel line transfer time of 6 μs per phase were employed. We used the drive system with the option of XCAM's 2-channel CDS card, where with the combination of headboard gain and CCD output node responsivity, the system noise for EM gain = 1× is dominated by the noise on the 14-bit ADC (rather than the CCD itself). However, operating with a maximum amplification gain of ∼200 we were able to routinely operate with an effective readout noise of 0.8 e$^-$ rms. This low effective noise was important in order to minimize the CTI (from both small optical signals and ^{55}Fe X-rays) within the multiplication register. Once optimized, we kept these bias conditions consistent for pre- and post-analyses. Similarly, the same Rϕ2HV (this voltage controls the multiplication gain) was consistent in both scenarios.

The amplifier responsivity and conversion gain were measured in order to calculate the system calibration, DN/e^-, as follows:

$$\frac{DN}{e^-} = \frac{V}{e^-} \cdot \frac{DN}{V},$$

(2)

Device 1: Parallel Irradiation **Device 2: Parallel & Serial Irradiation** **Comparison of traps Pre-/post-irradiation**
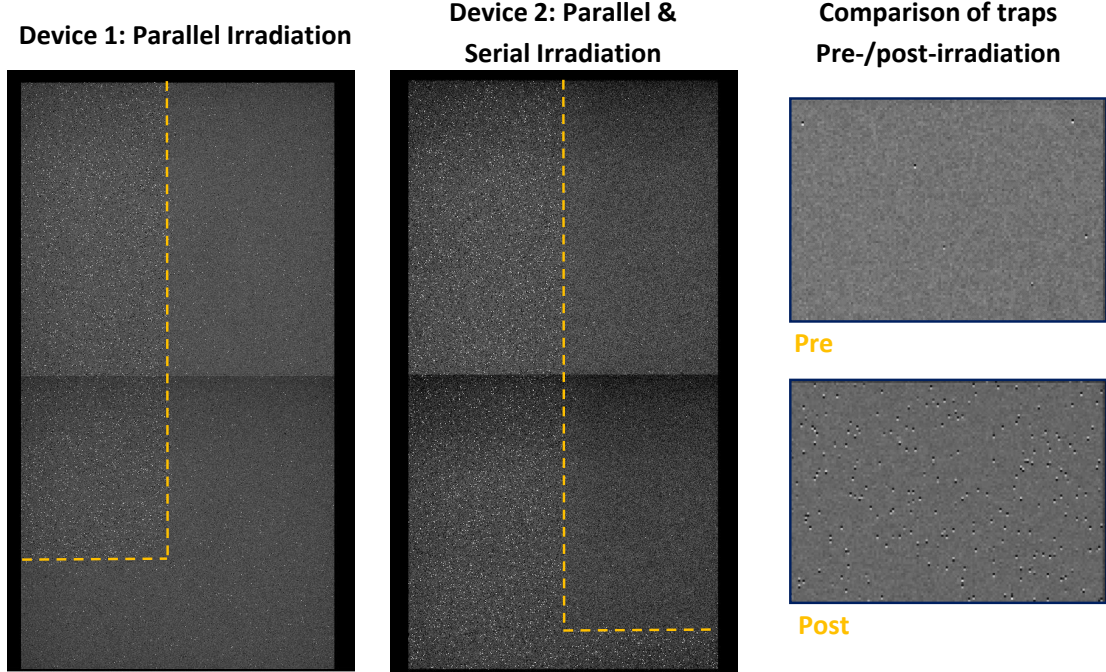
Pre

Post

Figure 3. Basic pocket pumping that was carried out in order to highlight the un-irradiated and irradiated regions of device 1 (left) and device 2 (center). We also show a comparison trapping site (right), highlighting a region of 90 × 50 pixels in the image area. In all cases, it is clear that the irradiated regions (within the dashed boxes) contain a much higher density of dipoles.

where V/e^- is the amplifier responsivity, and DN/V is the conversion gain, k-gain. We note that DN/e^- is the system calibration^{-1}. This calculation was necessary since it provided the signal level as measured from the Phase I device and system electronics and was essential for measurements later. Obtaining these parameters prior to irradiation was also a good indication of a change to the output electronics after the radiation tests were carried out. An ^{55}Fe X-ray source was used for this component of calibration.

5.2.3 Radiation Results

Here we present displacement damage radiation results for the CCD201. This is the first study to be carried out with a CCD201 in assessing performance degradation of this kind. We can confirm that both CCD201 EMCCD devices were fully functional after irradiation and experienced the degree of degradation in multiplication gain, dark current, CIC and charge transfer, that has been previously reported by other CCD sensors (e.g. Srour et al. 2013[24]) irradiated to a similar dose. We summarize the key performance degradation below, and show comparison results for each device in Table 4:

- Each device was fully functional following irradiation to 2.5×10^9 protons cm^{-2} (10 MeV equivalent).

- No significant change in the multiplication gain was observed (for an unbiased irradiation at ambient temperature).

- No significant change in the parallel CIC was observed (for an unbiased irradiation at ambient temperature).

- There was an IMO dark current increase by a factor of ~ 2.

- For low signal parallel CTI (~ 8 e$^-$), there was a degradation by a factor of ~ 5. The serial CTI appears to be dominated by the EM register and interaction with surface states for the operating conditions that were used. The extended pixel edge response, EPER, was used for low signal CTI measurements, and an ^{55}Fe X-ray source was used for high signal CTI measurements.

Table 4. Summary of pre- and post-irradiation test results for both CCD201 EMCCD devices. Any degradation factor that is left blank we consider to be inconsistent.

Parameter	Device 1 Pre-Irradiation	Device 1 Post-Irradiation	Device 2 Pre-Irradiation	Device 2 Post-Irradiation	Degradation [factor]
Multiplication Gain	238 ± 7	202 ± 6	237 ± 8	237 ± 8	...
Eff. Read Noise (e^- pix^{-1})	0.85 ± 0.04 [Par.]	0.98 ± 0.06 [Par.]	0.70 ± 0.07 [Par. + Serial]	0.91 ± 0.04 [Par. + Serial]	~ 1.2
Par. I$_{DK}$ (e^- pix^{-1} sec^{-1})	(7.13 ± 0.49) $\times 10^{-5}$	(1.22 ± 0.06) $\times 10^{-4}$	(3.195 ± 0.50) $\times 10^{-5}$	(5.75 ± 0.44) $\times 10^{-5}$	~ 1.8
Par. CIC (e^- pix^{-1} fr^{-1})	(4.47 ± 0.24) $\times 10^{-2}$	(4.86 ± 0.26) $\times 10^{-2}$	(8.80 ± 0.38) $\times 10^{-3}$	(9.90 ± 0.10) $\times 10^{-3}$	...
^{55}Fe Par. CTI	(5.14 ± 3.90) $\times 10^{-6}$	(4.05 ± 0.54) $\times 10^{-5}$	(1.23 ± 0.59) $\times 10^{-6}$	(3.07 ± 0.08) $\times 10^{-5}$	~ 10
^{55}Fe Serial CTI (Conv. register)	(1.05 ± 1.36) $\times 10^{-6}$	(2.04 ± 2.66) $\times 10^{-6}$	(1.73 ± 1.49) $\times 10^{-6}$	(1.08 ± 0.67) $\times 10^{-5}$	...
^{55}Fe Serial CTI (EM register)	$(1.19 \pm 0.01)^{\dagger}$ $\times 10^{-4}$	$(6.82 \pm 0.01)^{\dagger}$ $\times 10^{-5}$	(1.69 ± 0.01) $\times 10^{-4}$	(1.83 ± 0.01) $\times 10^{-4}$	~ 1.12
EPER Par. CTI	(1.13 ± 0.20) $\times 10^{-4}$	(5.40 ± 0.80) $\times 10^{-4}$	(9.26 ± 0.70) $\times 10^{-5}$	(3.94 ± 0.45) $\times 10^{-4}$	~ 5
EPER Serial CTI	(2.37 ± 0.70) $\times 10^{-4}$	(2.06 ± 0.22) $\times 10^{-4}$	(1.73 ± 0.21) $\times 10^{-4}$	(2.32 ± 0.38) $\times 10^{-4}$	...

†Device 1 did not have the EM register irradiated. However, the CTI has been reduced by a factor of ~ 1.7. This may be because of a decrease in multiplication gain that was observed for the device during post-irradiation testing. The total amount of signal would thus be smaller passing through the EM register and so less interaction with surface traps would occur. Acronyms/abbreviations: Par. = parallel; CTI = Charge Transfer Inefficiency; EPER = Extended Pixel Edge Response.

- Initial results suggest that serial CTI of the EM register has some dependence on the size of the signal being transferred as well as values for ϕDC and Rϕ2HV – the multiplication register DC bias and the high voltage clock.

Standard pocket pumping (Janesick 2001[9]) was employed which provides the means of probing trap sites due to displacement damage, where pixels were clocked in the forward direction and then subsequently in the opposite direction. We highlight again, that since the CCD201 device is designed to be operated in a 2-phase mode with charge only flowing forwards, each of the four phases are independently connected and therefore the device can be operated as a 4-phase device, albeit provided that one considers the impact of the implants on the clocking. As a result of this process, a pair of bright and dark pixels are now present signaling a trapping site, and can otherwise be known as a 'dipole'. Note that all of the trap populations will not be present as a result of the pumping cycle described above. This is because trapping efficiencies are a function of temperature and also

parallel line transfer timing, and each pumping cycle will only probe a certain area of the pixel. Furthermore, the pocket pumping technique used to generate the images as shown in Figure 3 did not probe 100% of the pixel, where we estimate <50% was probed - this is a tentative estimate since it is difficult to know the effect of fringing fields within a pixel. Work is on-going to probe a larger area of the pixel, which is difficult based on the presence of barrier implants. We refer the reader to Hall et al. (2014),[10–12] Wood et al (2014),[13] and Murray et al. (2012),[14,15] for in-depth studies of trap pumping for radiation damaged devices.

5.2.4 Significance of Results for the AFTA CGI

The results from the Phase I radiation study are encouraging when comparing the BOL and EOL detector performance relative to the requirements for the AFTA CGI. Based on current models that predict planetary yield as function of integration time, the most dominant sources of noise are dark current, CIC and CTI. After annealing that followed the Phase I radiation testing, we can report that the CCD201 measured dark current at operational temperatures of 165 K (IMO) passes the AFTA CGI requirement both before and after a DDD of 2.5×10^9 protons cm^{-2} – reflecting an EOL dose in L2 for 10 mm of tantalum shielding. Running at this temperature may affect the CTI under high gain conditions, and these effects are currently being investigated at JPL. Moreover, we can report no measurable increase in CIC within measurement error for pre- and post-irradiation of both the parallel section or the serial register for this unbiased, room temperature irradiation under Phase I. The results of CTI are still being considered, and the operating conditions of the device will play a vital role in optimizing this for the AFTA CGI.

5.2.5 Phase II Irradiation Plan

The Phase II irradiation study took place at the Helios-3 beamline in Harwell, UK, and was the first of its kind for the CCD201 for the reasons outlined below. This new plan commenced on June 01, 2015, where testing ended in August, 2015, and consisted of:

1) A pre-irradiation characterization of two science-grade CCD201s.

2) Four separate irradiation and characterizations at the following proton fluences: 1.0×10^9, 2.5×10^9, 5.0×10^9 and 7.5×10^9 protons cm^{-2}, that reflect the full range of radiation doses that a sensor would undergo during a 6 year flight in L2, by considering both tantalum and aluminum shielding of varied thicknesses (see Figure 2).

3) During the irradiation process at Harwell, the science grade sensor was maintained at a temperature of 165 K for all fluences, and was kept at this temperature during characterization in order to avoid annealing the effects of damage. A vacuum chamber was designed to operate in the Harwell beamline for this reason (Gow et al. 2015[25]).

4) The CCD was powered on during irradiation in order to investigate a positive flat-band shift as is expected in flight.

5) Post-irradiation characterization of each sensor.

Subsequent analysis of the radiation damaged sensors at JPL will further reveal the effects of annealing on the device following characterization at Harwell. Additionally, thermal cycling testing will also be carried out.

By assessing the sensor's radiation damage at a consistent cryogenic temperature, the density of defects and populations of the various trap species are expected to be different when compared to a room temperature irradiation, subsequently impacting dark current and CTI. We believe that this study, coupled with what was learned from Phase I, will be an accurate representation of what an EMCCD will undergo in orbit by considering the effects of displacement damage.

6. CONCLUSIONS

Here we present performance characterization of the CCD201-20 EMCCD that has been baselined for the AFTA CGI. This characterization has been carried out for BOL conditions, as well as conditions that reflect the space

environment of WFIRST-AFTA at the EOL of a 6 year flight in L2, specifically, displacement damage due to protons assuming a 10 mm tantalum shield. In the case of BOL characterization to meet the AFTA CGI detector requirements, we use the Nüvü Cameras EMN2 camera system with the CCCP controller, which uses highly tuned clocking to achieve sub-electron read noise, dark current of order 5×10^{-4} e$^-$ pix $^{-1}$ sec^{-1} at 188 K in IMO, and CIC of order 10^{-3} e$^-$ pix $^{-1}$ fr^{-1}. The measurement of initial radiation-induced performance degradation was carried out at the PSI in Switzerland using generic drive electronics from XCAM Ltd, and parameters such as multiplication gain, dark current, CIC and CTI, were assessed, as well as their impact on the AFTA CGI application. We report degradation of dark current of a factor of ∼1.8, which still meets AFTA CGI requirements for a temperature of 165 K at EOL. Similarly, no degradation of CIC was observed following room temperature irradiation, and we are still assessing the effect of charge transfer degradation of a factor of ∼1.12 in the EM register, and ∼5 in the parallel section. A second phase of the radiation study commenced in June, 2015 and these results will be released in early 2016.

ACKNOWLEDGMENTS

REFERENCES

1. R. T. Demers, F. Dekens, R. Calvet, et al., "Requirements and design reference mission for the WFIRST/AFTA coronagraph instrument", *Proc. SPIE*, in press (2015).
2. R. Kohley, P. Garé, C. Vétel, et al., "Gaia's FPA: sampling the sky in silicon", *Society of Photo-Optical Instrumentation Engineers (SPIE) Conference Series*, **8442**, 2012.
3. L. K. Harding, R. T. Demers, M. Hoenk, et al., "Technology Advancement of the CCD201-20 EMCCD for the WFIRST-AFTA Coronagraph Instrument: sensor characterization and radiation damage", *JATIS*, in press (2015).
4. P. Jerram, P. J. Pool, R. B. et al., "The llccd: low-light imaging without the need for an intensifier," in *Sensors and Camera Systems for Scientific, Industrial, and Digital Photography Applications II*, *Proc. SPIE* **4306**, pp. 178–186, 2001.
5. J. Hynecek, "Impactron - A New Solid State Image Intensifier", *IEEE Trans. on Electron Devices*, **48**, 10, 2001.
6. O. Daigle, J. L. Gach, C. Guillaume, et al., "CCCP: a ccd controller for counting photons," in *Society of Photo-Optical Instrumentation Engineers (SPIE) Conference Series*, *Proc. SPIE* **7014**, p. 6, 2008.
7. I. S. McLean, "Electronic Imaging in Astronomy," in *Praxis Publishing Ltd, Chichester*, **ISBN 978-3-540-76582-0**, 2008.
8. H. Michaelis, T. Behnke, S. Mottola, et al., "Investigations on performance of Electron Multiplied CCD detectors (EMCCDs) after radiation for observation of low light star-like objects in scientific space missions," *Proc. SPIE Sensors, Systems, and Next-Generation Satellites XVII*, **8889**, 2013.
9. J. R. Janesick, "Scientific charge-coupled devices," in *SPIE Optical Engineering Press*, **xvi 906**, 2001.
10. D. J. Hall, N. J. Murray, A. D Holland, et al., "Determination of in situ trap properties in CCDs using a "single-trap pumping" technique," *IEEE Transactions on Nuclear Science*, **61**, pp. 1826-1833, 2014.
11. D. J. Hall, N. J. Murray, J. P. D. Gow, et al., "Studying defects in the silicon lattice using CCDs," *Journal of Instrumentation*, **9(12)**, article no. C12004, 2014.

12. D. J. Hall, N. J. Murray, J. P. D. Gow, et al., "In situ trap parameter studies in CCDs for space applications," *In: High Energy, Optical, and Infrared Detectors for Astronomy VI*, **22-27 June**, 2014.

13. D. Wood, D. Hall, N. Murray, et al., "Studying charge-trapping defects within the silicon lattice of a p-channel CCD using a single-trap "pumping" technique," *Journal of Instrumentation*, **9**, article no. C12028, 2014.

14. N. J. Murray, D. J. Burt, A. D. Holland, et al., "The relationship between pumped traps and signal loss in buried channel CCDs," *In UV/Optical/IR Space Telescopes and Instruments: Innovative Technologies and Concepts VI*, **25-26 August**, 2013.

15. N. J. Murray, A. D. Holland, J. P. D. Gow, et al., "Mitigating radiation-induced charge transfer inefficiency in full-frame CCD applications by 'pumping' traps," *In High Energy, Optical, and Infrared Detectors for Astronomy V*, **1-6th July**, 2012.

16. J. P. D. Gow, N. Murray, A. Holland, et al., "Assessment of space proton radiation-induced charge transfer inefficiency in the CCD204 for the Euclid space observatory," *Journal of Instrumentation*, **7**, C01030, 2012.

17. R. Massey, T. Schrabback, O. Cordes, et al., "An improved model of charge transfer inefficiency and correction algorithm for the Hubble Space Telescope," *MNRAS*, **439**, 887, 2014.

18. T. M. Jordan, "NOVICE: A Radiation Transport/Shielding Code, Experimental and Mathematical Physics Consultation", $1983 - 2006$.

19. W. Shockley, and W. T. Jr. Read, "Statistics of the Recombinations of Holes and Electrons," *Physical Review*, **87(5)**, pp. 835-842, 1952.

20. D. J. Hall, A. D Holland, N. J. Murray, et al., "Modelling charge transfer in a radiation damaged Charge Coupled Device for Euclid," *In: High Energy, Optical, and Infrared Detectors for Astronomy V*, **Proc. of SPIE**, **8453**, 2012.

21. H. Israel, R. Massey, T. Prod'homme, et al., **in prep**, *private communication.*

22. N. Bush, D. Hall, A. Holland, et al., "The impact of radiation damage on photon counting with an EMCCD for the WFIRST-AFTA coronagraph," *Proc. SPIE*, in press (2015).

23. J. F. Ziegler, M. D. Ziegler and J. P. Biersack, "SRIM The stopping and range of ions in matter," *Nuclear Instruments and Methods in Physics Research Section B: Beam Interactions with Materials and Atoms*, **268 $(11-12)$**, p. $1818 - 1823$.

24. J. R. Srour, C. J. Marshall, and P. W. Marshall, "Review of Displacement Damage Effects in Silicon Devices," *IEEE Trans. Nucl. Sci.,*, **50**, 3, 2003.

25. J. P. D. Gow, P. H. Smith, P. Pool, et al., "Proton Irradiation of a CCD236 Swept Charge Device at Cryogenic Temperature and the Subsequent Annealing," *Journal of Instrumentation*, **10**, C01037, 2015.